The 2021 Mw 7.2 Haiti Earthquake: Rupture of a Blind Thrust Fault Revealed by Space Geodetic Observations

Hidayat Panuntun

Geomatics Laboratory, Department of Earth Technology, Vocational College, Universitas Gadjah Mada, Indonesia

Corresponding author: Hidayat Panuntun. Email: hidayat.panuntun@ugm.ac.id

Key points:

- The 2021 Haiti earthquake ruptured a north-dipping fault and was characterized by a combined left-lateral strike-slip and reverse slip
- Features of the preferred source model are inconsistent with the Enriquillo–Plantain Garden Fault's characteristics
- The Enriquillo–Plantain Garden Fault is probably not the seismogenic fault responsible for the 2021 Haiti earthquake

Plain Language Summary

An earthquake occurs due to the permanent shifting of a fault at a depth. Determining the causative fault responsible for the earthquake is important to improve our understanding of how the earth's surface deformed. This study focuses on the 2021 Haiti earthquake that jolted the southern region of Haiti on 14 August 2021. The surface deformation due to the 2021 Haiti earthquake imaged by the Sentinel-1 data is used to infer the fault geometry and the slip during the mainshock. Since the epicenter of this earthquake is located relatively close to the Enriquillo–Plantain Garden fault zone, one might think that the EPGF is the causative fault. However, characteristics of the preferred source model estimated in this study did not match with those of the EPGF, suggesting an earthquake ruptured fault other than the Enriquillo–Plantain Garden fault.

Abstract

On 14 August 2021, a large earthquake struck the southern region of Haiti. The epicenter of this earthquake is located relatively close to the Enriquillo–Plantain Garden Fault (EPGF) zone, a major active fault with a strike-slip mechanism in the southern part of Hispaniola. The Sentinel-1 data is utilized to investigate the seismogenic fault responsible for the 2021 Haiti earthquake. The Bayesian inversion and the aftershock distribution indicated that the mainshock ruptured a north-dipping fault, buried at a depth of ~10.4 km from the earth's surface. The preferred slip model showed that the rupture did not reach the surface and was confined at a depth of ~8 km to ~33 km. These characteristics are inconsistent with those of the EPGF, indicating that the EPGF is probably not the seismogenic fault responsible for the 2021 Haiti earthquake. Instead, results showed that the 2021 Haiti earthquake ruptured an unmapped blind fault.

1. **Introduction**

On 14 August 2021, a devastating earthquake struck the southwestern region of Haiti at 12:29:08 (UTC). Tectonically, Haiti is located at the western region of the Hispaniola Island, bisected by two major left-lateral strike-slip fault systems: (1) the Septentrional-Oriente fault (hereafter referred to as SOF) zone in the north and (2) the Enriquillo–Plantain Garden fault (hereafter refer to as EPGF) zone in the south, forming complex Trans-Haitian fold-and-thrust belts in central Haiti (e.g., Possee et al., 2019) (Figure 1a). This island is located on the northern Caribbean plate boundary that separates the Caribbean plate from the North American plate. The regional tectonic of the Northern Caribbean plate boundary is then dominated by an oblique collision where the Caribbean plate moves in the east-northeast direction at a rate of about 19 mm/yr relative to the North American plate (É. Calais et al., 2016).

The United States Geological Survey (USGS) has reported that the hypocenter of the 2021 Haiti earthquake is located in the southern region of Hispaniola at 18.434°N and 73.482°W with a focal depth of 10 km (Figure 1). Historically, three M-7 class earthquakes have occurred in the southern region of Hispaniola in 2010, 1770, and 1751 (e.g., Prentice et al., 2010). Epicenters of these three earthquakes are located relatively close to the EPGF zone (Figure 1b). As a major fault system in the region, the EPGF is initially thought to be the seismogenic fault responsible for these three events. However, previous studies showed that the 2010 earthquake ruptured a fault other than the EPGF (e.g., E. Calais et al., 2010; Hashimoto et al., 2011), while the epicenters of the two other events remain poorly constrained (e.g., Bakun et al., 2012). The epicenter of the 2021 earthquake is also located relatively close to the EPGF zone. This situation can cause difficulties in determining what faults are likely responsible for the 2021 event.

Geodetic observation techniques such as the global navigation satellite system (GNSS) and the interferometric synthetic aperture radar (InSAR) have proven to be an essential tool in observing the coseismic surface deformation. Both GNSS and InSAR techniques can provide measurements with a high level of precision. However, the InSAR technique has a higher spatial resolution because the GNSS technique only provides pointwise measurement data. The low spatial resolution data of the GNSS measurement sometimes prevents us from fully understanding the source of an earthquake-related deformation. Unlike the GNSS data, the InSAR data has been successfully used by previous studies to reveal hidden features of the seismogenic fault (e.g., Ghayournajarkar & Fukushima, 2020; Nie et al., 2018), including the earthquake's source's mechanism (e.g., L. He et al., 2019; Panuntun, 2021; Ragon et al., 2021) and the geometric complexity of both large- (e.g., H. Chen et al., 2021) and medium-sized earthquakes (e.g., Kobayashi et al., 2018; Wang et al., 2018). The main purpose of this study is to estimate the causative fault responsible for the 2021 Haiti earthquake, using the Sentinel-1 SAR data from both ascending and descending tracks to image the coseismic surface deformation due to the 2021 Haiti earthquake. The observed surface deformation is used to constrain the geometry of the causative fault responsible for the earthquake and the slip distribution.

1. **Geodetic data: Observation and processing strategy**

The InSAR data in TOPS (Terrain Observation by Progressive Scans) modes imaged by Sentinel-1A satellites were used to capture the coseismic signal of the 2021 Haiti earthquake. Descending and ascending image pairs obtained from paths 4 and 142 were used to generate coseismic interferograms (Figure 1b, Table S1). Interferograms, which were formed from Single Look Complex products, were processed using the GMTSAR software (Sandwell et al., 2011). For each interferogram pair, the enhanced spectral diversity method was used to improve the alignment of master and slave images (e.g., Shirzaei et al., 2017). A 30-meter resolution of the Shuttle Radar Topography Mission version 3 Digital Elevation Model (SRTM v.3 DEM) was used to remove topographic phase artifacts. Topographic-free interferograms were filtered using an adaptive power spectrum filter (Goldstein & Werner, 1998) and unwrapped using the minimum cost flow SNAPHU algorithm (C. W. Chen & Zebker, 2000). To better illustrate the ground deformation in the earth's surface, unwrapped interferograms were then converted to line-of-sight (LOS) displacements and geocoded to WGS84 geographic coordinates. Here, LOS displacements represent the range change in the satellite view toward or away from the sensor.

1. **Modeling Approach**

   (a) **Fault Geometry**

Space-based geodetic observations such as InSAR and GNSS are capable of providing a millimeter level of precision (e.g., Elliott et al., 2016). However, unlike the GNSS observation, InSAR can only generate a one-dimensional motion along the satellite sensor. The surface deformation recorded by the InSAR measurement only provides information on whether the earth's surface is moving away or toward the satellite sensor. Consequently, the LOS displacement pattern cannot be easily used to presume the fault geometry and the earthquake's source's mechanism, thus causing difficulty in the interpretation of the physical process or ambiguity in the modeling result.

Various additional information including the spatial distribution of the aftershock and surface break due to the mainshock are required to infer the geometry of the causative fault responsible for the earthquake. The absence of a report about the field geology survey makes the information about the surface crack due to the mainshock limited. Additionally, there are only a few aftershocks observed one month after the mainshock. Therefore, the Bayesian modeling approach with uniform slip proposed by Bagnardi and Hooper (2018) is used to carefully estimate the geometry of the fault plane. In this approach, the posterior probability distribution of source model parameters and uncertainties were sampled using the Markov chain Monte Carlo and Metropolis-Hasting algorithm through 10^6 iterations (Figure S1). To reduce the computation burden, input interferograms were down-sampled using a quad-tree method (e.g., Jónsson et al., 2002).

The optimal model shows a fault plane with a strike of 263° and a dip of 57.5°

buried at a depth of 10.4 km from the earth's surface (Table 1). This result is consistent with the source moment tensor solution from various agencies. Focal mechanism solution issued by various agencies provided two nodal planes with different strike and dip directions. In this way, most previous InSAR-based coseismic studies have to simulate at least two or more different fault planes to safely infer the seismogenic fault responsible for the mainshock (e.g., Sun et al., 2018; Tang et al., 2021). The result showed that the Bayesian approach can estimate the strike and dip direction of the nodal plane. The physical mechanism of the aftershock is still subject to debate. Nonetheless, its distribution can be used to infer the fault geometry (e.g., Yukutake & Iio, 2017). The optimal fault model estimated by the Bayesian approach is consistent with the spatial distribution of aftershock relocations by USGS. Therefore, a combination of the InSAR observation and aftershock distribution helps us to judge the causative fault of the earthquake without having to make any additional simulation for another possible rupture plane.

1. **Coseismic slip model**

Strike and dip angles estimated from the Bayesian approach are then used to image a more detailed rupture slip distribution at a depth through an inversion on a discretized fault plane. Here, an inversion procedure similar to that used by Panuntun (2021) is employed. The best fit fault plane obtained in chapter 3.1 is extended along the strike and dip direction to avoid bias due to the edge effect. The fault plane is divided into 22 x 17 small rectangular patches of ~3 km x ~3 km. Down-sampled LOS displacements from ascending and descending orbit paths 4 and 142, respectively, are used to invert the slip at a depth. A kernel matrix related to the surface displacement response due to slip at a certain depth is built using the Okada (1992) formula. The inversion algorithm is constructed to solve the slip at the fault interface by minimizing the following function:

$$\mathbf{s}(\mathbf{m}) = (\mathbf{d}-\mathbf{G}\mathbf{m})^{\mathbf{T}}\,\mathbf{E}^{-\mathbf{1}}\,(\mathbf{d}-\mathbf{G}\mathbf{m}) + {}^{\mathbf{2}}\mathbf{m}^{\mathbf{T}}\,(\mathbf{B}^{\mathbf{T}}\mathbf{B})\,\mathbf{m} \quad (1)$$

where m is the slip vector matrix, G is the Green's function matrix, d is the LOS displacement data, E is the measurement error described by Lohman and Simons (2005), B is the Laplacian second-order smoothness matrix, and α^2 is the hyperparameter. The hyperparameter α^2 is selected based on the minimization of ABIC (Akaike's Bayesian information criterion) form (e.g., Ide, 2015)

$$\mathrm{ABIC}\ (\ {}^{\mathbf{2}}) = \mathbf{N}\log\mathbf{s}\ (\mathbf{m}) - \mathbf{M}\log(\ {}^{\mathbf{2}}) + \log\left|\mathbf{G}^{\mathbf{T}}\mathbf{E}^{-\mathbf{1}}\mathbf{G} + {}^{\mathbf{2}}\mathbf{B}^{\mathbf{T}}\mathbf{B}\right| \quad (2)$$

where N and M are the number of data and parameters, respectively.

1. **Result and Discussion**

Coseismic interferograms have a similar fringe pattern close to the earthquake's epicenter (Figure 2a and 2b), inferring a dominant uplift motion in the region (e.g., Wang et al., 2020). At a greater distance from the earthquake's epicenter, interferograms exhibit a different pattern, indicating that the surface deformation in the region is dominated by a horizontal displacement (e.g., Huang & Huang, 2018). The LOS displacement from both ascending and descending interferograms detected an uplift pattern located about 20–30 km to the west of the earthquake's epicenter. The maximum LOS displacement from the ascending orbit is 1.5 times larger than the LOS displacement from the descending orbit. Specifically, the decreasing range observed from ascending and descending orbits are up to 0.45 m and 0.29 m (Figure 2c and 2d), respectively. It is difficult to obtain a straightforward interpretation of the earthquake's source's mechanism from the LOS displacement. However, satellite viewing geometries implied that the surface deformation due to this earthquake is dominated by a westward motion. Results of the InSAR observation suggest that both strike-slip and dip-slip motions have a predominant control at different regions.

A 2.5-D displacement calculation is used to verify the interpretation of coseismic deformation fringes and LOS displacements (Fujiwara et al., 2000). Theoretically, a three-dimensional surface displacement can be calculated using at least three LOS displacements from three different viewing geometries (e.g., Yu et al., 2017). Most previous studies (e.g., P. He et al., 2019; Hu et al., 2014; Jo et al., 2017) used the InSAR data from multiple platforms to generate a 3D surface displacement. Since this study only used two LOS displacements from two different viewing geometries, the author does not try to decompose LOS displacements into 3D surface displacements. Moreover, the direction of the Sentinel-1 orbital track is almost parallel to the north-south direction. Thus, it is difficult to detect the reliable contribution of the north-south component to the surface displacement. Here, a 2.5-D displacement that consist of E-W and U-D motions can be related to the LOS displacements U through the following equation (e.g., Hu et al., 2014):

$$\mathbf{U} = -\mathbf{ue}.\cos(\,).\sin(\,) + \mathbf{uu}.\mathbf{cos}(\,) \quad (3)$$

where φ is the azimuth of the satellite heading vector, θ is the incident angle, and ue and uu are the E-W and U-D components of the surface displacement, respectively. In this study, ue and uu are estimated by inverting the LOS displacements of the ascending and descending orbit path 4 and 142, respectively. In the vicinity of the rupture area, a 2.5-D displacement field shows a dominant uplift motion close to the earthquake's epicenter with a maximum magnitude of 0.54 m. A dominant eastward motion is detected at a greater distance from the epicenter with a maximum amplitude of 0.41 m (Figure S2). The result confirms the interpretation that the dip-slip motion plays a role in the eastern side of the ruptured fault, while the strike-slip motion has significant control on the western side.

Figure 3 shows the coseismic slip model, which is calculated using the hyper-parameter α^2 that gives the minimum value in Equation (2) (Figure S3). Estimated LOS displacements show relatively good agreement with the observed data (Figure 4). Residuals of the LOS displacement from the ascending path 4 and descending path 142 are 14 cm and 7 cm, respectively. The preferred solution shows that the rupture did not reach the surface and confined at a depth of ~8 km to ~33 km with a maximum slip of 3.79 m. The total InSAR-based moment is estimated up to 8.37 x 10^{19} Nm, which is equal to a moment magnitude of Mw = ~7.2 (assuming a uniform rigidity of 40 GPa). The estimated moment magnitude is in good agreement with previously published seismic moments from various agencies. The preferred solution shows that the seismogenic fault is characterized by the combination of the left-lateral strike-slip and reverse slip. A coseismic slip distribution on the discretized fault plane exhibits a dominant reverse slip at the shallow patch close to the epicenter and mainly a left-lateral strike-slip at the western side and a deeper patch. Given the reported hypocenter and the preferred coseismic model, it suggests that the rupture started at a depth of ~10 km and propagated unilaterally to the southwest along the fault plane.

The preferred coseismic model shows that the major slip patch is identified at a depth of 14 km to 18 km and did not propagate up to the shallow part. This feature then causes the absence of a surface break due to the mainshock. The absence of a surface rupture related to the seismogenic fault of the 2021 Haiti earthquake indicates that this event ruptured a blind fault. The Bayesian approach estimated that the mainshock ruptured a north-dipping fault with a dip angle of 57.5°. It is worth noting that the EPGF is a left-lateral strike-slip south-dipping fault with a near-vertical (>60°) dip angle (e.g., Douilly et al., 2013; Mercier de Lépinay et al., 2011; Prentice et al., 2010). This study identified that the characteristics of the preferred source model are inconsistent with the characteristics of the EPGF. It can be inferred that the EPGF is probably not the seismogenic fault responsible for the 2021 Haiti earthquake. Instead, a thrusting fault that lies almost parallel to the EPGF is the causative fault of the event.

The preferred rupture fault plane is consistent with the crustal structure of western Hispaniola reported by teleseismic studies (e.g., Corbeau et al., 2017). This fault system could be a part and is located at the southwestern-most extension of the Trans-Haitian belt, a fold-and-thrust belt bounded by the SOFZ to the north and EPGF to the south (e.g., Possee et al., 2019). A north-dipping fault plane with a dip angle of ~57.5° is similar to the Leogane fault, a causative fault of the 2010 Haiti earthquake (e.g., E. Calais et al., 2010; Hashimoto et al., 2011; Hayes et al., 2010). Additionally, the 2010 Haiti earthquake and the 2021 Haiti earthquake have a similar source mechanism, i.e., a combination of strike-slip and reverse slip on the north-dipping fault plane. The causative fault of the 2010 Haiti earthquake is also located at the southernmost of the Trans-Haitian belt. The epicenter of the 2021 event is located ~75 km to the west of the 2010 event. These similarities suggest that both 2021 and 2010 events might be lo-

cated within the same fault systems. In this way, the seismogenic fault of the 2021 event is the western extension of the seismogenic fault of the 2010 event.

An unruptured fault segment is then identified if the 2010 and 2021 earthquakes occurred in the same fault system. This fault segment is located between those two rupture zones. It has been widely accepted that the coseismic stress change imparted by the earthquake could increase seismicity in the surrounding area, promoting the occurrence of another big earthquake in the neighboring fault segment. To assess the potential seismic hazard of the unruptured segments, the Coulomb stress change induced by the 2021 event is calculated using the Coulomb 3.3 software (assuming a friction coefficient of 0.4) (Toda et al., 2011). The result shows that the unruptured fault segment is located under increased stress (Figure S4), enhancing the chance of occurrence of large earthquakes in the future. However, given the fact that there is no large earthquake recorded in this region since two and a half centuries ago increases the uncertainty of the recurrence time. If the 2021 Haiti earthquake is counted as the characteristic event in this fault segment with an annual rate of about 17–19 mm/yr (É. Calais et al., 2016), it takes about 200 to 223 years to accumulate the same amount of slip released by this earthquake. This is almost similar to the time lapse of the last two major earthquakes in the Hispaniola region (in 1751 and 1770).

Most of the aftershock epicenters are spread and found at the northern side of the surface projection of the preferred fault with only a few of them located on the southern side. A major aftershock distribution in only one side of the plate interface is found in some cases of megathrust earthquakes, such as the 2012 Costa Rica earthquake (e.g., Yue et al., 2013), the 2007 Pisco earthquake (e.g., A. Sladen et al., 2010), and the 2003 Tokachi earthquake (e.g., Miyazaki & Larson, 2008). Traditionally, strong asperities at the shallow plate interface play an important role in promoting seismicity in and around the ruptured fault interface (e.g., Dmowska & Lovison, 1992). However, Anthony Sladen and Trevisan (2018) argued that instead of strong asperities, a major aftershock at both sides of the fault interface would occur only if the earthquake rupture broke up to the surface. In the other words, the lack of aftershock distribution in the southern side of the preferred fault might be due to the slip that did not propagate all the way to the surface. Additionally, since the causative fault of the 2021 event is sub-parallel and close to the EPGF, this study believes that the EPGF might play a role as a mechanical boundary that limits the aftershock distribution in the southern side.

1. Conclusion

Sentinel-1 TOPS imaging modes, which have a wide coverage area (up to 250 km) and a short revisit time (6–12 days), has been utilized to image the coseismic surface deformation due to the 2021 Haiti earthquake and to determine its source mechanism. The Bayesian approach suggested that the earthquake had ruptured a fault plane with a strike of 263° with a dip of 57.5° buried at a depth of 10.4 km from the earth's surface. The preferred source model showed a major slip patch with a maximum slip of ~3.79 m located at a depth of 14

km to 18 km. The total InSAR-based moment is estimated up to 8.37 x 10^{19} Nm. Assuming a uniform rigidity of 40 GPa, the InSAR-based moment is equal to a moment magnitude of Mw = ~7.2. Characteristics of the preferred coseismic slip model are inconsistent with the characteristics of the EPGF. It suggested that the 2021 Haiti earthquake occurred on a different plane from the Enriquillo–Plantain Garden fault (EPGF) system. Instead, the causative fault of the 2021 event might be located within the same fault system as the 2010 Haiti earthquake, a major event that occurred ~75 km to the east of the 2021 earthquake epicenter.

1. **Open Research**

I am grateful for the free data access of Sentinel-1 which provided by the European Space Agency (ESA) and were downloaded from the Alaska Satellite Facility (https://search.asf.alaska.edu/#/). The Geodetic Bayesian Inversion Software (GBIS) used to estimate deformation source parameters can be accessed from https://comet.nerc.ac.uk/downloadgbis/. GMT software (https://www.generic-mapping-tools.org/download/) is used to generate figures in this manuscript (Wessel et al., 2019).

1. **References**

https://doi.org/10.1029/2018GC007585

https://doi.org/10.1785/0120110077

https://doi.org/10.1038/ngeo992

https://doi.org/10.1016/j.crte.2015.10.007

https://doi.org/10.1364/JOSAA.17.000401

https://doi.org/10.3390/rs13163327

https://doi.org/10.1016/j.tecto.2017.04.029

https://doi.org/10.1016/0040-1951(92)90049-C

https://doi.org/10.1785/0120120303

https://doi.org/10.1038/ncomms13844

https://doi.org/10.1029/1999gl011291

https://doi.org/10.1186/s40623-020-01190-6

https://doi.org/10.1029/1998gl900033

https://doi.org/10.1038/ngeo1115

https://doi.org/10.1038/ngeo977

https://doi.org/10.1016/j.tecto.2019.228216

https://doi.org/10.1016/j.rse.2019.111321

https://doi.org/10.1016/j.earscirev.2014.02.005

https://doi.org/10.1029/2018GL080821

https://doi.org/10.1038/s41598-017-06018-0

https://doi.org/10.1785/0120000922

https://doi.org/10.1016/j.tecto.2017.12.001

https://doi.org/10.1029/2004gc000841

https://doi.org/10.1029/2011GL049799

https://doi.org/10.1029/2007gl032309

https://doi.org/10.1186/s40623-018-0826-4

https://doi.org/10.1785/BSSA0820021018

https://doi.org/10.1016/j.tecto.2021.228814

https://doi.org/10.1029/2018TC005364

https://doi.org/10.1038/ngeo991

https://doi.org/10.1029/2020GL090704

https://doi.org/10.1029/2011eo280002

https://doi.org/10.1002/2017GL072663

https://doi.org/10.1029/2009JB006429

https://doi.org/10.1016/j.epsl.2017.12.006

https://doi.org/10.5194/nhess-20-831-2020

https://doi.org/10.1002/2017gl076421

https://doi.org/10.3390/rs13081573

http://pubs.er.usgs.gov/publication/ofr20111060

https://doi.org/10.1029/2019EA000966

https://doi.org/10.1785/0220180211

https://doi.org/10.3390/rs9111194

https://doi.org/10.1002/jgrb.50379

https://doi.org/10.1186/s40623-017-0650-2

Bagnardi, M., & Hooper, A. (2018). Inversion of Surface Deformation Data for Rapid Estimates of Source Parameters and Uncertainties: A Bayesian Approach. *Geochemistry, Geophysics, Geosystems, 19*(7), 2194-2211. Bakun, W. H., Flores, C. H., & ten Brink, U. S. (2012). Significant Earthquakes on the

Enriquillo Fault System, Hispaniola, 1500–2010: Implications for Seismic Hazard. *Bulletin of the Seismological Society of America, 102*(1), 18-30. Calais, E., Freed, A., Mattioli, G., Amelung, F., Jónsson, S., Jansma, P., et al. (2010). Transpressional rupture of an unmapped fault during the 2010 Haiti earthquake. *Nature Geoscience, 3*(11), 794-799. Calais, É., Symithe, S., Mercier de Lépinay, B., & Prépetit, C. (2016). Plate boundary segmentation in the northeastern Caribbean from geodetic measurements and Neogene geological observations. *Comptes Rendus Geoscience, 348*(1), 42-51. Chen, C. W., & Zebker, H. A. (2000). Network approaches to two-dimensional phase unwrapping: intractability and two new algorithms. *Journal of the Optical Society of America A, 17*(3), 401-414. Chen, H., Qu, C., Zhao, D., Ma, C., & Shan, X. (2021). Rupture Kinematics and Coseismic Slip Model of the 2021 Mw 7.3 Maduo (China) Earthquake: Implications for the Seismic Hazard of the Kunlun Fault. *Remote Sensing, 13*(16), 3327. Corbeau, J., Rolandone, F., Leroy, S., Guerrier, K., Keir, D., Stuart, G., et al. (2017). Crustal structure of western Hispaniola (Haiti) from a teleseismic receiver function study. *Tectonophysics, 709*, 9-19. Dmowska, R., & Lovison, L. C. (1992). Influence of asperities along subduction interfaces on the stressing and seismicity of adjacent areas. *Tectonophysics, 211*(1), 23-43. Douilly, R., Haase, J. S., Ellsworth, W. L., Bouin, M. P., Calais, E., Symithe, S. J., et al. (2013). Crustal Structure and Fault Geometry of the 2010 Haiti Earthquake from Temporary Seismometer Deployments. *Bulletin of the Seismological Society of America, 103*(4), 2305-2325. Elliott, J. R., Walters, R. J., & Wright, T. J. (2016). The role of space-based observation in understanding and responding to active tectonics and earthquakes. *Nature Communications, 7*, 13844. Fujiwara, S., Nishimura, T., Murakami, M., Nakagawa, H., Tobita, M., & Rosen, P. A. (2000). 2.5-D surface deformation of M6.1 earthquake near Mt Iwate detected by SAR interferometry. *Geophysical Research Letters, 27*(14), 2049-2052. Ghayournajarkar, N., & Fukushima, Y. (2020). Determination of the dipping direction of a blind reverse fault from InSAR: case study on the 2017 Sefid Sang earthquake, northeastern Iran. *Earth, Planets and Space, 72*(1), 64. Goldstein, R. M., & Werner, C. L. (1998). Radar interferogram filtering for geophysical applications. *Geophysical Research Letters, 25*(21), 4035-4038. Hashimoto, M., Fukushima, Y., & Fukahata, Y. (2011). Fan-delta uplift and mountain subsidence during the Haiti 2010 earthquake. *Nature Geosci, 4*(4), 255-259. 10.1038/ngeo1115. Hayes, G. P., Briggs, R. W., Sladen, A., Fielding, E. J., Prentice, C., Hudnut, K., et al. (2010). Complex rupture during the 12 January 2010 Haiti earthquake. *Nature Geoscience, 3*(11), 800-805. He, L., Feng, G., Li, Z., Feng, Z., Gao, H., & Wu, X. (2019). Source parameters and slip distribution of the 2018 Mw 7.5 Palu, Indonesia earthquake estimated from space-based geodesy. *Tectonophysics, 772*, 228216. He, P., Wen, Y., Xu, C., & Chen, Y. (2019). Complete three-dimensional near-field surface displacements from imaging geodesy techniques applied to the 2016 Kumamoto earthquake. *Remote Sensing of Environment, 232*, 111321. Hu, J., Li, Z. W., Ding, X. L., Zhu, J. J., Zhang, L., & Sun, Q. (2014). Resolving three-dimensional surface displacements from InSAR measurements: A review. *Earth-Science Reviews, 133*, 1-17. Huang, M.-H., & Huang, H.-H. (2018). The Complexity of the 2018 Mw

6.4 Hualien Earthquake in East Taiwan. *Geophysical Research Letters, 45*(24), 13,249-213,257. Ide, S. (2015). 4.09 - Slip Inversion. In G. Schubert (Ed.), *Treatise on Geophysics (Second Edition)* (pp. 215-241). Oxford: Elsevier.Jo, M.-J., Jung, H.-S., & Yun, S.-H. (2017). Retrieving Precise Three-Dimensional Deformation on the 2014 M6.0 South Napa Earthquake by Joint Inversion of Multi-Sensor SAR. *Scientific Reports, 7*(1), 5485. Jónsson, S., Zebker, H., Segall, P., & Amelung, F. (2002). Fault Slip Distribution of the 1999 Mw 7.1 Hector Mine, California, Earthquake, Estimated from Satellite Radar and GPS Measurements. *Bulletin of the Seismological Society of America, 92*(4), 1377-1389. Kobayashi, T., Morishita, Y., & Yarai, H. (2018). SAR-revealed slip partitioning on a bending fault plane for the 2014 Northern Nagano earthquake at the northern Itoigawa–Shizuoka tectonic line. *Tectonophysics, 733*, 85-99. Lohman, R. B., & Simons, M. (2005). Some thoughts on the use of InSAR data to constrain models of surface deformation: Noise structure and data downsampling. *Geochemistry, Geophysics, Geosystems, 6*(1), Q01007. Mercier de Lépinay, B., Deschamps, A., Klingelhoefer, F., Mazabraud, Y., Delouis, B., Clouard, V., et al. (2011). The 2010 Haiti earthquake: A complex fault pattern constrained by seismologic and tectonic observations. *Geophysical Research Letters, 38*(22). Miyazaki, S., & Larson, K. M. (2008). Coseismic and early postseismic slip for the 2003 Tokachi-oki earthquake sequence inferred from GPS data. *Geophysical Research Letters, 35*(4), L04302. Nie, Z., Wang, D.-J., Jia, Z., Yu, P., & Li, L. (2018). Fault model of the 2017 Jiuzhaigou Mw 6.5 earthquake estimated from coseismic deformation observed using Global Positioning System and Interferometric Synthetic Aperture Radar data. *Earth, Planets and Space, 70*(1), 55. Okada, Y. (1992). Internal deformation due to shear and tensile faults in a half-space. *Bulletin of the Seismological Society of America, 82*(2), 1018-1040. Panuntun, H. (2021). Geodetic slip model of the November 26, 2019 Albania earthquake estimated from Sentinel-1 TOPS interferometry. *Tectonophysics, 807*, 228814. Possee, D., Keir, D., Harmon, N., Rychert, C., Rolandone, F., Leroy, S., et al. (2019). The Tectonics and Active Faulting of Haiti from Seismicity and Tomography. *Tectonics, 38*(3), 1138-1155. Prentice, C. S., Mann, P., Crone, A. J., Gold, R. D., Hudnut, K. W., Briggs, R. W., et al. (2010). Seismic hazard of the Enriquillo–Plantain Garden fault in Haiti inferred from palaeoseismology. *Nature Geoscience, 3*(11), 789-793. Ragon, T., Simons, M., Bletery, Q., Cavalié, O., & Fielding, E. (2021). A Stochastic View of the 2020 Elazığ Mw 6.8 Earthquake (Turkey). *Geophysical Research Letters, 48*(3), e2020GL090704. Sandwell, D., Mellors, R., Tong, X., Wei, M., & Wessel, P. (2011). Open radar interferometry software for mapping surface Deformation. *Eos, Transactions American Geophysical Union, 92*(28), 234-234. Shirzaei, M., Bürgmann, R., & Fielding, E. J. (2017). Applicability of Sentinel-1 Terrain Observation by Progressive Scans multitemporal interferometry for monitoring slow ground motions in the San Francisco Bay Area. *Geophysical Research Letters, 44*(6), 2733-2742. Sladen, A., Tavera, H., Simons, M., Avouac, J. P., Konca, A. O., Perfettini, H., et al. (2010). Source model of the 2007 Mw 8.0 Pisco, Peru earthquake: Implications for seismogenic behavior of subduction megathrusts. *Journal of Geophysical Research: Solid Earth, 115*(B2). Sladen,

A., & Trevisan, J. (2018). Shallow megathrust earthquake ruptures betrayed by their outer-trench aftershocks signature. *Earth and Planetary Science Letters, 483*, 105-113. Styron, R., García-Pelaez, J., & Pagani, M. (2020). CCAF-DB: the Caribbean and Central American active fault database. *Nat. Hazards Earth Syst. Sci., 20*(3), 831-857. Sun, J., Yue, H., Shen, Z., Fang, L., Zhan, Y., & Sun, X. (2018). The 2017 Jiuzhaigou Earthquake: A Complicated Event Occurred in a Young Fault System. *Geophysical Research Letters, 45*(5), 2230-2240. Tang, X., Guo, R., Xu, J., Sun, H., Chen, X., & Zhou, J. (2021). Probing the Fault Complexity of the 2017 Ms 7.0 Jiuzhaigou Earthquake Based on the InSAR Data. *Remote Sensing, 13*(8), 1573. Toda, S., Stein, R. S., Sevilgen, V., & Lin, J. (2011). *Coulomb 3.3 Graphic-rich deformation and stress-change software for earthquake, tectonic, and volcano research and teaching-user guide* (2011-1060). Retrieved from Reston, VA: Wang, S., Xu, C., Li, Z., Wen, Y., & Song, C. (2020). The 2018 Mw 7.5 Papua New Guinea Earthquake: A Possible Complex Multiple Faults Failure Event With Deep-Seated Reverse Faulting. *Earth and Space Science, 7*(3), e2019EA000966. Wang, S., Xu, C., Xu, W., Yin, Z., Wen, Y., & Jiang, G. (2018). The 2017 Mw 6.6 Poso Earthquake: Implications for Extrusion Tectonics in Central Sulawesi. *Seismological Research Letters, 90*(2A), 649-658. Wessel, P., Luis, J. F., Uieda, L., Scharroo, R., Wobbe, F., Smith, W. H. F., & Tian, D. (2019). The Generic Mapping Tools Version 6. *Geochemistry, Geophysics, Geosystems, 20*(11), 5556-5564. 10.1029/2019GC008515Yu, L., Yang, T., Zhao, Q., Liu, M., & Pepe, A. (2017). The 2015–2016 Ground Displacements of the Shanghai Coastal Area Inferred from a Combined COSMO-SkyMed/Sentinel-1 DInSAR Analysis. *Remote Sensing, 9*(11), 1194. Yue, H., Lay, T., Schwartz, S. Y., Rivera, L., Protti, M., Dixon, T. H., et al. (2013). The 5 September 2012 Nicoya, Costa Rica Mw 7.6 earthquake rupture process from joint inversion of high-rate GPS, strong-motion, and teleseismic P wave data and its relationship to adjacent plate boundary interface properties. *Journal of Geophysical Research: Solid Earth, 118*(10), 5453-5466. Yukutake, Y., & Iio, Y. (2017). Why do aftershocks occur? Relationship between mainshock rupture and aftershock sequence based on highly resolved hypocenter and focal mechanism distributions. *Earth, Planets and Space, 69*(1), 68.

Table 1. Comparison of fault parameters for the 2021 Haiti earthquake

Reference	**Depth (km)**	**Dip (Degree)**	**Strike (Degree)**	**Longitude**	**Latitude**	**Mw**	
This Study	$10.38^{+13.42}_{+6.44}$	$57.5^{+68.8}_{+20.7}$	263^{+299}_{+246}	$-73.58^{-73.65}_{-73.52}$	$18.41^{+18.44}_{+18.39}$	7.2	
GFZ	NP1	15	56	264	−73.45	18.33	7.1
	NP2		57	149			
NEIC	NP1	15.5	51	266	−73.48	18.42	7.2
	NP2		65	153			
GCMT	NP1	10	64	266	−73.63	18.51	7.2
	NP2		53	154			

Note: Superscript and subscript notations attached to each estimated parameter

indicated the lower bound and upper bound with 97.5% confidence intervals, respectively.

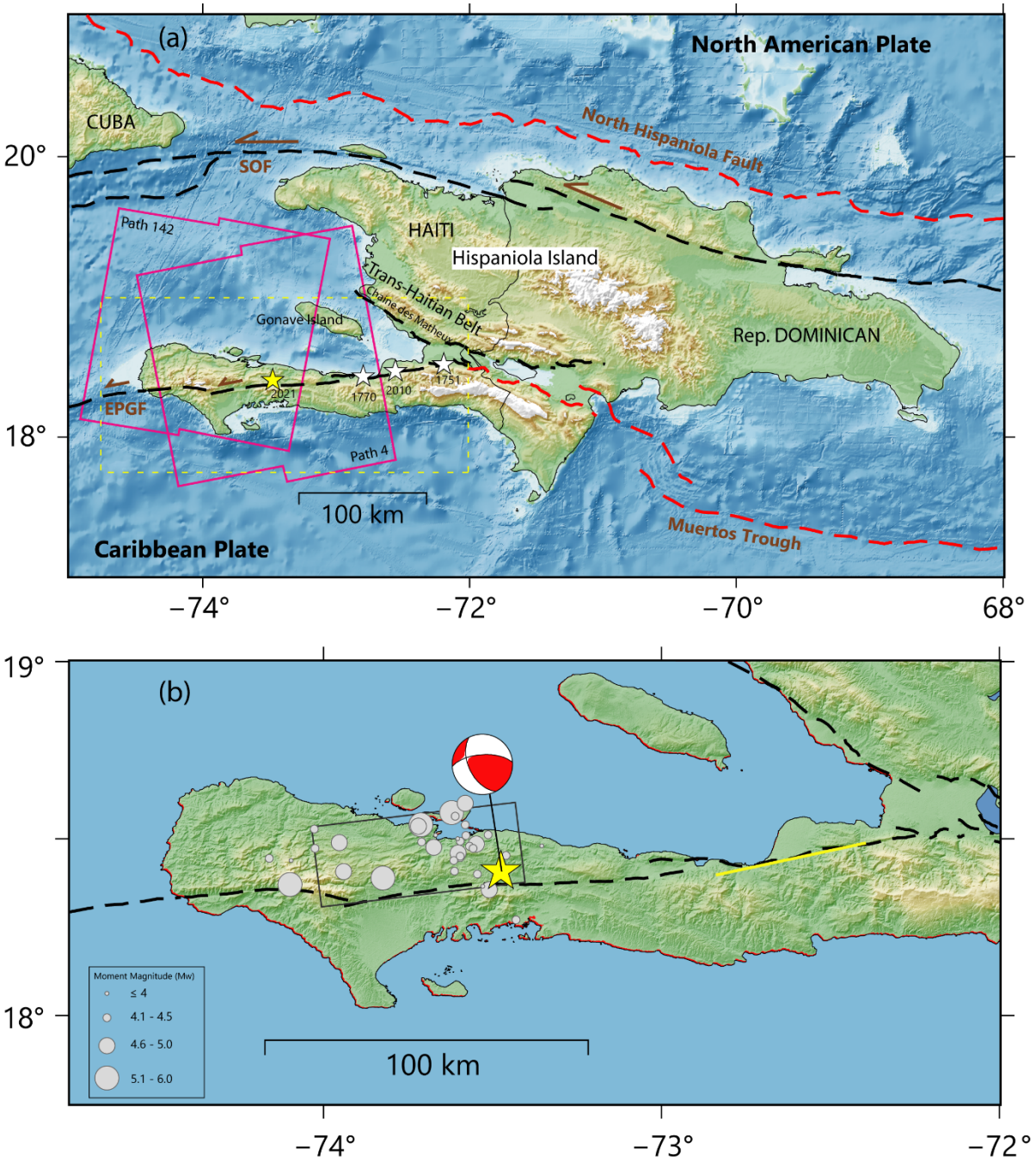

Figure 1. Tectonic setting around the 2021 Haiti earthquake's epicenter. (a) Major active fault in and around Hispaniola Island obtained from Styron et al. (2020). White stars represent the location of the M-7 class earthquake that occurred close to the EPGF. The yellow star shows the 2021 event's epicenter. Red dashed lines represent thrust fault systems, while black dashed lines indicate strike-slip fault systems. (b) 2021 mainshock and its aftershocks. The gray circle shows the aftershock one month following the mainshock. The yellow line denotes the surface projection of the preferred fault model for the 2010 Haiti earthquake (E. Calais et al., 2010).

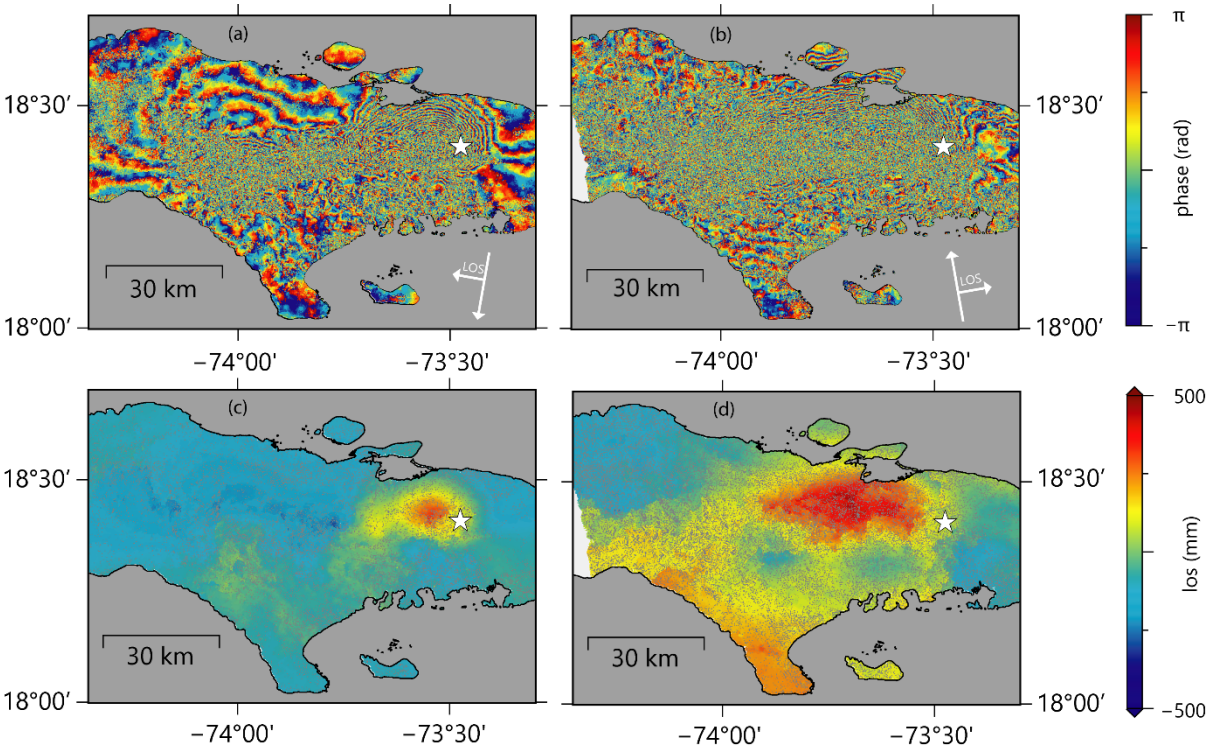

Figure 2. Coseismic interferograms of (a) descending Sentinel-1 path 142 and (c) its line-of-sight (LOS) displacement. Coseismic interferograms of (b) ascending Sentinel-1 path 4 and (d) its line-of-sight (LOS) displacement. The white star denotes the earthquake's epicenter.

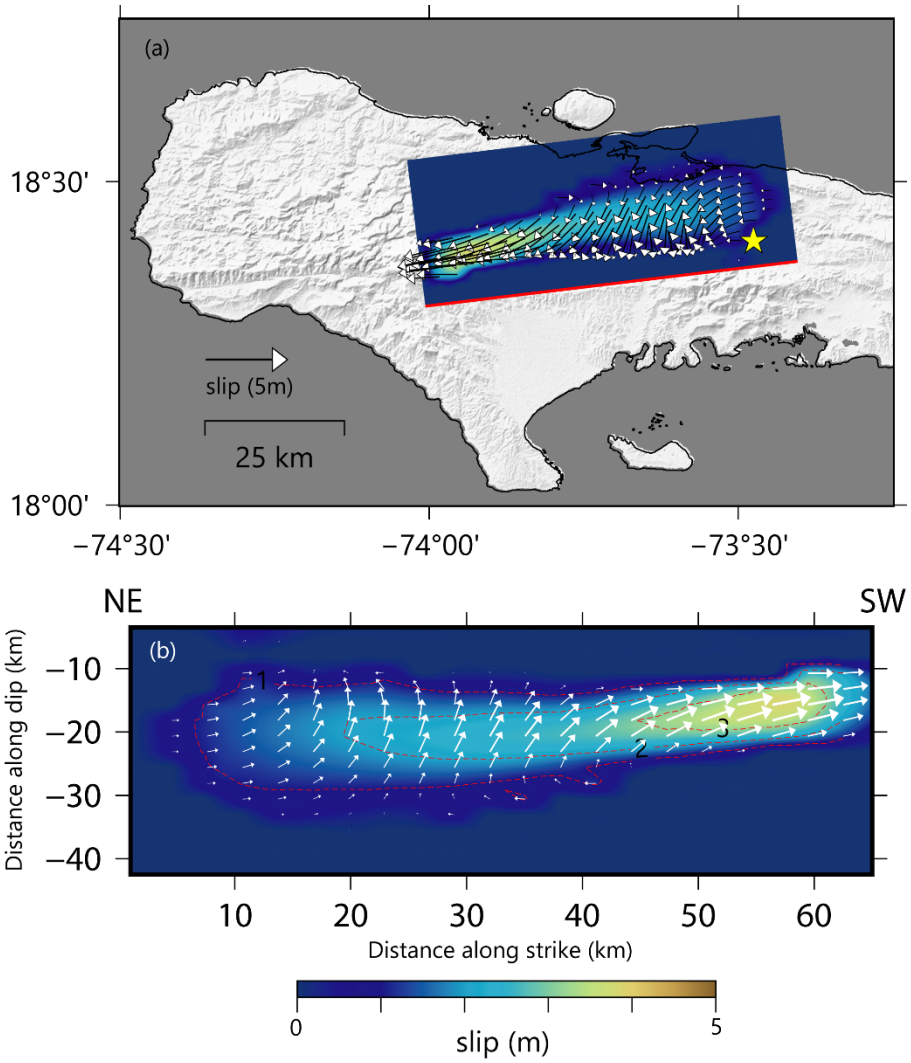

Figure 3. Coseismic slip distribution of the 2021 Haiti earthquake. (a) The white star indicates the earthquake's epicenter. The solid red line indicates the upper fault edge. (b) Red dashed lines show the slip contour at 1-m intervals.

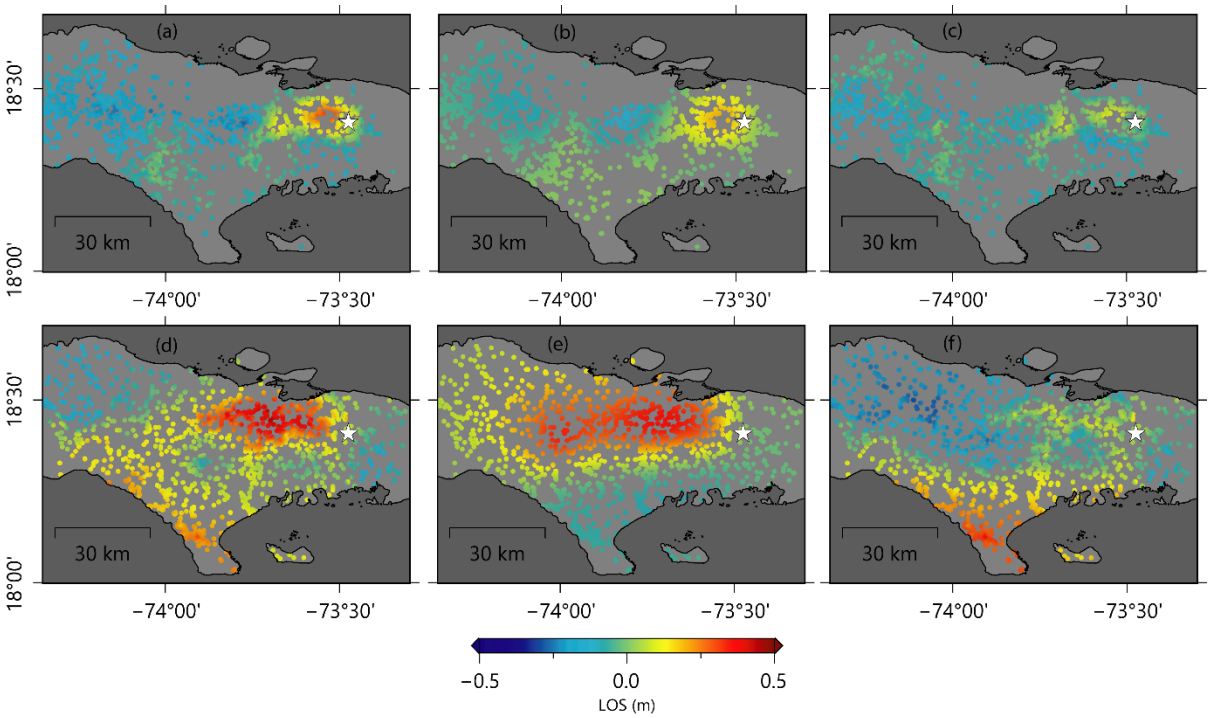

Figure 4. Down-sampled LOS displacement and its residual. (a) Observed, (b) modeled, and (c) residual (observed—modeled) of the LOS displacement Sentinel-1 descending path 142. (d) Observed, (e) modeled, and (f) residual (observed–modeled) of the LOS displacement Sentinel-1 ascending path 4.